Photo-oxidation of Methanol Using MoO₃/TiO₂: Catalyst Structure and Reaction Selectivity

Y. C. Liu,*,1 G. L. Griffin,* S. S. Chan,†,2 and I. E. Wachs†

Department of Chemical Engineering and Materials Science, University of Minnesota, Minneapolis, Minnesota 55455; and †Corporate Research Science Laboratories, Exxon Research and Engineering Company, Annandale, New Jersey 08801

Laser Raman spectra, UV–visible spectra, and photo-catalytic activity measurements are described which show that supported MoO₃/TiO₂ catalysts prepared by impregnation possess a layer of surface molybdate species coordinated to the titania support. The saturation coverage of this surface molybdate monolayer corresponds to a surface density of ca. 4×10^{14} Mo atoms per cm² of TiO₂. The properties of this surface monolayer are markedly different from bulk MoO₃, as reflected in different vibrational frequencies for the surface molybdate species and for bulk MoO₃, and in the higher photo-catalytic activity of the surface molybdate relative to bulk MoO₃. The photo-efficiency of the TiO₂ catalyst containing the surface molybdate monolayer is about one-fifth of the photo-efficiency of pure TiO₂, but the selectivity for suppressing secondary oxidation reactions is significantly greater. The major photo-assisted oxidation product on TiO₂ is methyl formate, independent of methanol conversion. In contrast, the molybdate monolayer catalyst has nearly 100% selectivity for dimethoxymethane (the reversible condensation product of CH₂O + 2 CH₃OH) at low conversions. For both catalysts the selectivity of the primary oxidation step appears to be insensitive to the mode of excitation (i.e., thermal vs photo-assisted). Photo-induced changes in selectivity at a given conversion are due primarily to differences in adsorbate coverage at the different operating temperatures required to give equal conversion for dark vs light reactions. © 1985 Academic Press, Inc.

INTRODUCTION

Surface morphology has a major effect on the activity and selectivity of heterogeneous catalysts, especially for multicomponent catalysts such as those used for partial oxidation reactions. A variety of surface morphologies may be encountered with these catalysts, ranging from the homogeneous limit in which the surface composition reflects the composition of a bulk-phase alloy, to the completely segregated limit in which each component exists as crystallites of its own phase. Understanding the structure and chemical behavior of such multicomponent surfaces is a major

challenge in the area of partial oxidation catalysis, and in catalysis in general.

Recently our group at Minnesota has become interested in supported MoO₃/TiO₂ as a possible catalyst for selective photo-oxidation reactions. TiO₂ is well known as a photo-catalyst for the partial oxidation of alkanes, alkenes, and alcohols (1–5), but it has relatively poor selectivity for thermally catalyzed reactions (6, 7). In contrast, MoO₃ is selective for a number of partial oxidation reactions (8–10), but shows little intrinsic photo-activity (see below). Therefore we decided to investigate whether a properly prepared MoO₃/TiO₂ catalyst might combine the desired photo-activity and selectivity of the separate components.

A second reason for studying the MoO₃/TiO₂ system is to determine whether Mo forms a surface molybdate monolayer on TiO₂ (11–13). The existence of a surface

molybdate layer is already well documented for Mo supported on Al_2O_3 (*14*). For the case of MoO_3/TiO_2, a similar monolayer structure may be responsible for the improved thermal selectivity reported for partial oxidation of olefins and alcohols on these catalysts. Non-photo-assisted reactions that have been studied include the oxidation of toluene (*12*), butadiene (*15, 16*), isobutene (*16*), 2-propanol and CO (*11*), methanol (*6*), and ethanol (*13*), and NO reduction using NH_3 (*17, 18*).

The reaction we have chosen to study is the partial oxidation of CH_3OH. Alcohol oxidation is of general interest as a synthetic reaction, while methanol oxidation provides a simple enough example so that most of the intermediate products can be monitored. If the mechanism is written as a simple series reaction

$$CH_3OH \rightarrow CH_2O \rightarrow HCOOCH_3 \rightarrow$$
$$CO \rightarrow CO_2 \quad (1)$$
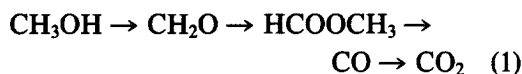
then the goal of our photooxidation research is to determine if it is possible to photo-excite the primary oxidation step (i.e., $CH_3OH \rightarrow CH_2O$) at low enough temperatures to suppress the rates of subsequent oxidation steps.

Our presentation of results and their subsequent discussion will be divided into two parts. In the results section we first describe the physical characterization of a series of MoO_3/TiO_2 catalysts with different Mo loadings. We then present the results of a series of activity and selectivity measurements for selected catalyst compositions, comparing light and dark reactions. Similarly in the discussion section we deal first with the surface morphology of the catalysts, and then with the probable reaction mechanism for CH_3OH oxidation.

EXPERIMENTAL

Catalysts were prepared by impregnating TiO_2 (Degussa P-25) with aqueous solutions containing different concentrations of $(NH_4)_6Mo_7O_{24}$. The TiO_2 support had a sur-

face area of ca. 50 m²/g, and contained 60% anatase and 40% rutile as determined by X-ray diffraction. The impregnated pastes (ca. 0.5 ml solution per gram TiO_2) were dried in air at 393 K overnight, calcined at 773 K for 4 h, and then ground to a fine powder.

X-Ray diffraction patterns were obtained with a Philips diffractometer using $CuK\alpha$ radiation and a diffracted beam monochromator. The diffraction measurements revealed that the anatase : rutile ratio of the TiO_2 support was not altered by the calcination treatment. Surface areas were determined using a standard BET apparatus with N_2 as the adsorbing gas. An average value of 47 ± 2 m²/g was obtained for all of the catalyst compositions studied up to 13.5 wt%, indicating that the TiO_2 support was stable at these calcination temperatures.

Raman spectra were obtained using a multichannel laser Raman spectrometer (*19, 20*). An Ar⁺ ion laser (Spectra Physics, Model 165) was tuned to the 514.5-nm line for excitation. The laser power at the sample location was set at 40 mW. The Raman spectrometer was a triple monochromator (Instruments SA, Model DL203) that was coupled to a cooled intensified photodiode array detector and an optical multichannel analyzer (Princeton Applied Research, Model OMA 2). The spectral resolution was 6 cm⁻¹.

UV–Visible absorbance spectra were obtained using a Cary 17-D spectrometer. Spectra were obtained in the direct transmission mode, using thin layers of catalyst resuspended from acetone onto NaCl windows.

The photoreactor used in these experiments is shown in Fig. 1. It consists of an aluminum body and a Suprasil window mounted with Teflon gaskets, and can be operated at atmospheric pressure and temperatures up to 473 K. The thin-layer design minimizes residence time, allows good temperature control, and provides a well-defined flow field for the reactant gas, at the expense of operating as an integral reactor at high conversions.
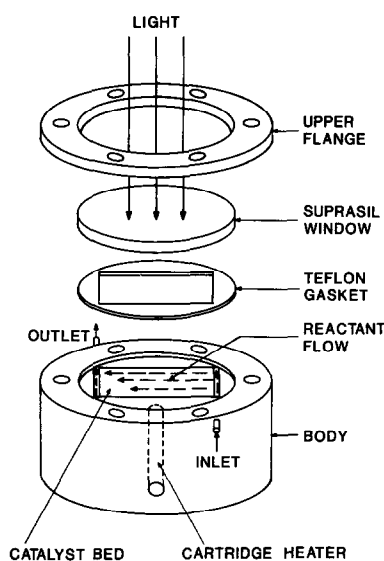
FIG. 1. Configuration of plug-flow thin-layer photoreactor used in this work.

The light source was a 100-W medium-pressure Hg arc lamp, with principle spectral output lines at 365, 545, 580, 435, and 405 nm, according to manufacturer's data. No attempt was made to calibrate the absolute intensity of the lamp; the relative intensity was controlled by changing the distance between the lamp and the photoreactor.

The catalyst samples were coated onto the illuminated surface of the photoreactor by deposition from a resuspended aqueous slurry. The amount of catalyst used was 100 mg, spread over 20 cm². Photo-activity measurements were obtained using a reactant mixture of 4% CH_3OH/22% O_2/74% He. Product analysis was performed using a gas chromatograph (Porapak T column, 4 ft. × ⅛ in., He carrier flow 20 cm³/min) with a flame ionization detector. The reactant residence time in the photoreactor was fixed at 0.2 min for all measurements reported here. The observed partial oxidation products included CH_2O, dimethoxymethane (DMM = $(CH_3O)_2CH_2$), methyl formate (MF = $HCOOCH_3$), and dimethyl ether (DME = $(CH_3)_2O$). We did not attempt to measure the yields of CO and/or CO₂ at high CH_3OH conversions; their sum could be estimated by applying a carbon balance over the remaining products.

The laser Raman spectra, X-ray diffraction patterns, and surface areas were obtained at Exxon. The catalyst preparation, UV–visible spectra, and catalytic activity measurements were performed at Minnesota.

RESULTS

I. Physical Characterization

The catalyst compositions studied in this work are listed in Table 1. Weight percentage loadings are calculated as (grams MoO_3)/(grams MoO_3 + grams TiO_2), based on concentration and quantity of solution used during the impregnation step. For reference we also list the effective surface concentration of Mo atoms per square centimeter of TiO_2 for each loading, based on the average measured BET surface area of 47 m²/g.

X-Ray diffraction. Diffraction patterns were obtained for samples containing 0.8 to 13.5 wt% MoO_3. Crystalline MoO_3 was detected only in the XRD patterns of the 7.5 and 13.5 wt% loadings. The absence of bulk-phase MoO_3 in the XRD patterns for the 0.8, 1.8, and 4.0 wt% loadings implies that for these samples the molybdenum oxide is present in either a noncrystalline state or as small crystallites of less than 4 nm in diameter. Additional information

TABLE 1

Catalyst Compositions Studied in This Work

wt% loading (MoO_3)/(MoO_3 + TiO_2)	Surface concentration (Mo atoms/cm² TiO_2)
0.3	2.8×10^{13}
0.8	7.0×10^{13}
1.9	1.6×10^{14}
4.0	3.6×10^{14}
7.5	6.8×10^{14}
13.5	1.3×10^{15}
44.0	6.5×10^{15}
66.0	1.7×10^{16}

about the state of molybdenum oxide at these low loadings is provided by other spectroscopic results presented below.

Laser Raman spectra. In Fig. 2 we show the laser Raman spectra over the frequency range from 750 to 1200 cm^{-1} for the five catalyst compositions mentioned above, and for unpromoted TiO$_2$. The sharp vibrational bands at 821 and 997 cm^{-1} seen for the 7.5 and 13.5 wt% MoO$_3$/TiO$_2$ catalysts are characteristic of bulk MoO$_3$ (*21*). The anatase phase of the TiO$_2$ support possesses a weak second-order feature at 794 cm^{-1} (*22*). The 0.8, 1.8, and 4.0 wt% catalysts, however, exhibit a broad Raman band between 900 and 1000 cm^{-1}. The peak of the broad Raman band shifts from 940 to 967 cm^{-1} as the molybdenum oxide loading increases. The position, shape, and loading-dependent shift of this band preclude its assignment to either crystalline MoO$_3$ or TiO$_2$. Instead, we associate the band with a surface molybdate species coordinated to the TiO$_2$ support.
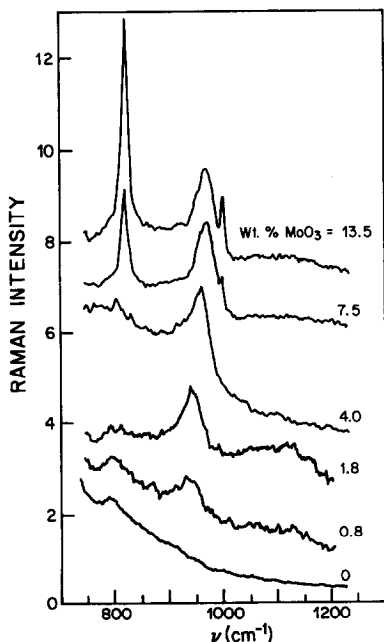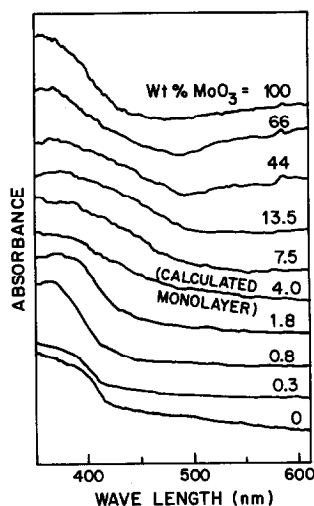

FIG. 3. UV–Visible absorbance spectra of MoO$_3$/TiO$_2$ catalysts for different Mo loadings. Evidence for surface oxide layer.

The Raman spectra of the 7.5 and 13.5 wt% catalysts also exhibit the broad band at 967 cm^{-1} assigned to the surface molybdate phase, in addition to the sharp bands at 821 and 998 cm^{-1} assigned to MoO$_3$ crystallites. However, the features of the broad Raman band of the surface molybdate phase remain constant for the 4.0, 7.5, and 13.5 wt% samples. This suggests that the coverage of the surface molybdate species reaches a saturation limit at a catalyst loading of about 4 wt% MoO$_3$/TiO$_2$.

UV–Visible spectra. In Fig. 3 we show the UV–visible spectra over the wavelength range 350–600 nm for all of the catalyst compositions listed in Table 1, and for pure TiO$_2$ and pure MoO$_3$. Pure TiO$_2$ shows an absorption edge at 420 nm, corresponding to the bulk TiO$_2$ band gap of 3.1 eV (*23*). As the Mo loading increases to 4.0 wt% MoO$_3$/TiO$_2$, corresponding to the range of loadings over which the surface molybdate Raman band became fully developed, the sharpness of the TiO$_2$ absorption edge degrades progressively. For the 4.0 wt% loading, the absorption edge is no longer directly apparent. Instead, the absorbance decreases continuously over the region 400 to 500 mn, suggesting a broadened distribu-

FIG. 2. Laser Raman vibrational spectra for MoO$_3$/TiO$_2$ catalysts for different Mo loadings. Evidence for surface oxide monolayer.

tion of absorption transitions over this energy range.

For loadings greater than 4.0 wt% MoO_3/TiO_2, the absorption spectrum from 400 to 500 nm remains essentially unchanged. This provides further evidence that the surface molybdate monolayer is completed at a loading of approximately 4.0 wt% MoO_3/TiO_2. A structureless increase in the baseline absorbance above 500 nm is observed, which we attribute to absorbance by MoO_3 crystallites. The spectrum of bulk MoO_3 is shown at the top of the figure. It shows a poorly defined absorption edge at 405 nm corresponding to the bulk MoO_3 band gap of 2.9 eV (23), and a slowly rising structureless absorbance above 450 nm.

Additional evidence for the assignment of the absorbance slope between 400 and 500 nm is given in Fig. 4, in which we compare the UV–visible spectra for pure TiO_2, pure Mo_3, the 4.0 wt% MoO_3/TiO_2 catalyst, and an 8.0% MoO_3/Al_2O_3 catalyst. The latter sample was prepared from Degussa Alon-C (surface area 100 m^2/g), using the same impregnation procedure as above. Previous laser Raman studies have shown that a surface molybdate monolayer is present on γ-Al_2O_3 at this loading (21).

The absorbance in the region 400–500 nm is essentially constant for the 8 wt% MoO_3/Al_2O_3 catalyst, in contrast to the monotonic decrease seen for the 4.0 wt% MoO_3/TiO_2 catalyst. Since both catalysts contain about a monolayer of surface molybdate species,
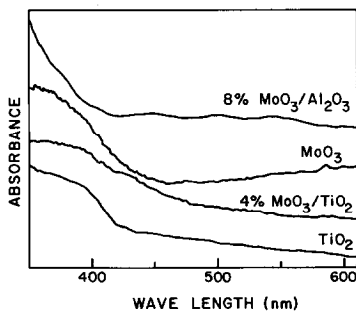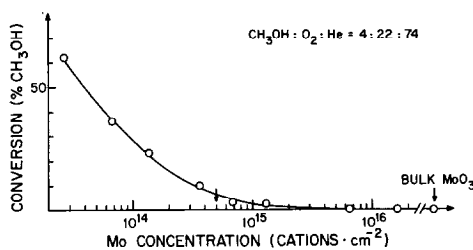

FIG. 5. Conversion of CH_3OH on illuminated MoO_3/TiO_2 catalysts as a function of Mo loading, for fixed light intensity and reactor temperature. Arrow indicates calculated monolayer coverage.

this suggests that the absorption transitions in this region are not intrinsic to surface molybdate species on all supports. Instead, we suggest that the absorbance in the region 400–500 nm may be due to sub-band gap transitions in the near-surface region of the TiO_2 support that are induced by the presence of the surface molybdate monolayer.

II. Kinetic Characterization

Two kinds of kinetic experiments were performed to probe the reaction characteristics of these catalysts. In the first set we measured the photo-conversion and major product yields for catalysts with different molybdena loadings, using a fixed reactor temperature (403 K) and light source distance (11 cm). In the second set (see below) we examined product yields as a function of conversion for selected catalyst compositions.

Catalyst loading studies. Figure 5 shows the photo-conversion of CH_3OH as a function of molybdena loading. Loadings are expressed as Mo atom concentration per square centimeter of TiO_2 surface area (cf. Table 1), using a logarithmic concentration axis to clearly display the entire range that was studied. Photo-conversion (vertical axis) is defined as the difference between the fractional conversion of CH_3OH measured with the light on and off. At 403 K, the dark conversion was negligible on TiO_2 and reached a maximum value of 6% for the 13.5 wt% loading.

FIG. 4. UV–Visible absorbance spectra comparison of MoO_3, TiO_2, MoO_3/TiO_2, and MoO_3/Al_2O_3 catalysts.

The highest conversions are obtained with low Mo loadings. This behavior is consistent with the high photo-efficiency expected for TiO_2. The photoconversion drops steadily as the Mo loading is increased, and there is no measurable photo-conversion for bulk MoO_3. We note, however, that most of the decrease in photo-conversion occurs over the range of loadings where the Raman and UV–visible data showed that the surface molybdate layer was being completed. This suggests that sites on the uncovered TiO_2 and the surface molybdate layer are kinetically distinguishable. The two types of site have different specific photo-efficiencies, with the surface molybdate layer sites being the less efficient type.

Further evidence that the surface molybdate layer becomes complete over the range of loadings up to approximately 4.0 wt% MoO_3/TiO_2 is seen in the major product yields for each loading. Figure 6 shows the relative photo-assisted yield of methyl formate (MF) observed for each catalyst loading, as measured directly from the difference between the GC peak areas recorded with the light on and off. Methyl formate is the major product observed for catalysts with low Mo loadings, and for pure TiO_2 (see below). The photo-yield of MF decreases for higher loadings, with most of the decrease again occurring over the range where the surface molybdate layer is being completed.
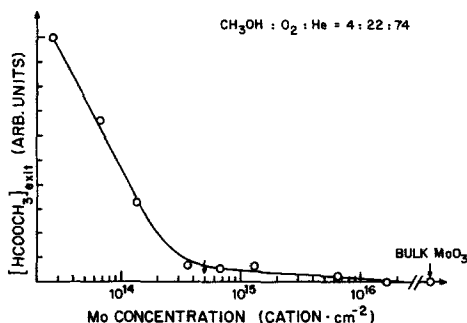

FIG. 6. Relative yield of methyl formate on illuminated MoO_3/TiO_2 catalysts as a function of Mo loading.
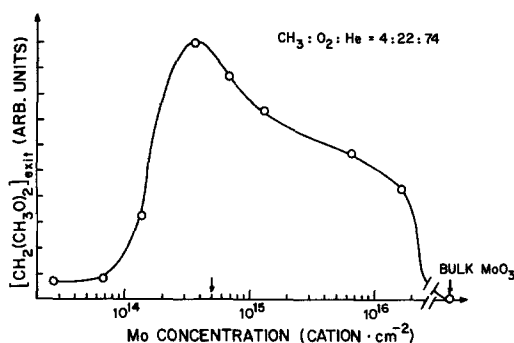

FIG. 7. Relative yield of dimethoxymethane on illuminated MoO_3/TiO_2 catalysts as a function of Mo loading.

Figure 7 shows the photo-yield of dimethoxymethane (DMM) observed for each loading. At 403 K, DMM rather than CH_2O is observed as the primary oxidation product (see below). The dependence on catalyst loading is markedly different from that seen for MF. The DMM yield is small for catalysts with low Mo loadings, and increases to a maximum near the loading where the surface molybdate layer is complete. This shows that DMM is the favored photo-product at sites on the surface molybdate layer. At higher loadings the DMM photo-yield decreases, and the yield drops to zero for pure MoO_3. This suggests that for loadings above monolayer coverage, the surface molybdate sites become partially blocked by MoO_3 crystallites which are themselves photo-inert.

Yield vs conversion studies. Two methods were used to vary the conversion, in order to separate thermally induced effects from photo-assisted effects. In the first method, we varied the conversion of the photo-controlled reaction by changing the distance between the light source and the photoreactor. In the second method we varied the conversion of the dark reaction by changing the reactor temperature. To achieve comparable conversions in the two sets of experiments, it was necessary to perform the thermal reactions in a separate tubular reactor that could be operated above 473 K.
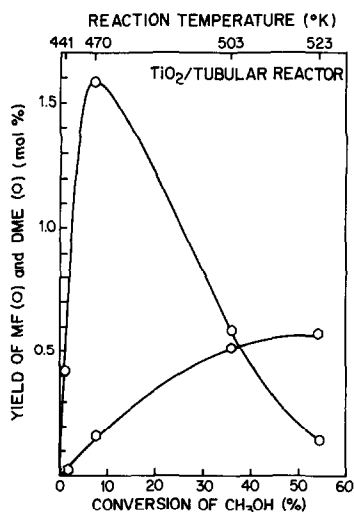
FIG. 8. Yields of intermediate products during thermally controlled CH_3OH oxidation using TiO_2 catalyst, as a function of CH_3OH conversion in tubular reactor.

In Fig. 8 we show the yields of all measurable intermediate products for the dark reaction on TiO_2. Here the yield is defined as the exit concentration of each product, divided by the inlet concentration of CH_3OH. The yields are plotted as a function of CH_3OH conversion, so that a tangent to the curve through the data points for each product has a slope equal to the instantaneous selectivity for that product. The temperature needed to achieve each indicated conversion is shown along the top axis.

For TiO_2, the dark reaction does not become measurable until 440 K. At this temperature, the only observed products are dimethyl ether (DME) and methyl formate (MF). Neither CH_2O nor DMM are observed, indicating that secondary oxidation occurs rapidly. The MF yield passes through a maximum at a CH_3OH conversion of only 10%, indicating that MF oxidation to CO or CO_2 is also fast relative to the primary oxidation rate.

For comparison, Fig. 9 shows the photoyields as a function of conversion for illuminated TiO_2 at 403 K. The distance between the light source and the sample needed to

achieve each conversion is listed along the top axis of the figure. We see that comparable conversions are obtained at substantially lower temperatures, and that MF is still the major product. However, the MF yield does not pass through a maximum, and there are significant yields of CH_2O and DMM. Thus the secondary oxidation steps have been significantly suppressed by operating at lower temperature. Also, there is no measurable photo-yield of DME.

The corresponding results for the surface molybdate catalysts are shown in Figs. 10–12. Figure 10 shows the product yields for the dark reaction on the 4.0 wt% MoO_3/TiO_2 catalyst. It should be remembered that this loading corresponds approximately to a complete monolayer of the surface molybdate species. Reaction occurs at much lower temperatures than on TiO_2, and both DMM and CH_2O products are seen in addition to MF and DME. The DMM yield passes through a maximum because its formation from CH_2O and two CH_3OH molecules becomes unfavorable at higher temperatures. The maximum in the CH_2O yield is attributed to the onset of secondary oxidation at higher temperatures.

Since the results in Fig. 8 showed that TiO_2 is very active for the thermally controlled oxidation of CH_2O, it seems possible
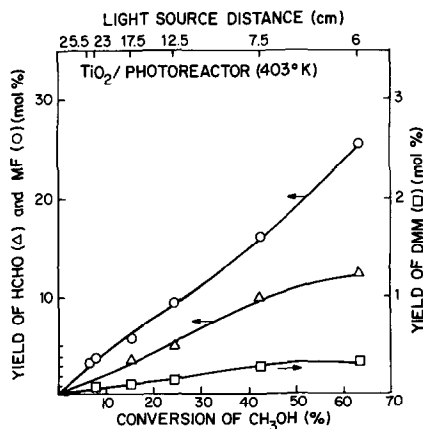

FIG. 9. Yields of intermediate products during photo-controlled CH_3OH oxidation using TiO_2 catalyst, as a function of CH_3OH conversion in photoreactor.
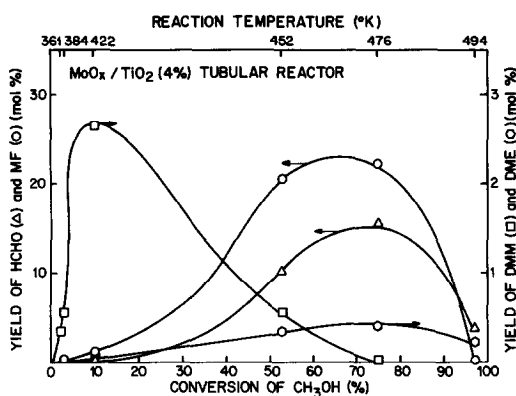
FIG. 10. Intermediate yields for thermally controlled CH_3OH oxidation using 4 wt% MoO_3/TiO_2 catalyst.

that the decay of the CH_2O yield at high conversions seen for the 4.0 wt% MoO_3/TiO_2 catalyst might be due to oxidation at exposed TiO_2 sites not completely covered by the surface molybdate layer. To test this possibility, we also examined the 13.5 wt% MoO_3/TiO_2 catalyst in detail. At this loading the surface molybdate monolayer should be complete, although at the expense of having MoO_3 crystallites present.

The yields for the dark reaction on the 13.5 wt% MoO_3/TiO_2 catalyst are shown in Fig. 11. The CH_2O yield increases monotonically for conversions up to 90%. This supports the idea that exposed TiO_2 is responsible for some of the MF formation seen with the 4.0 wt% catalyst. However,
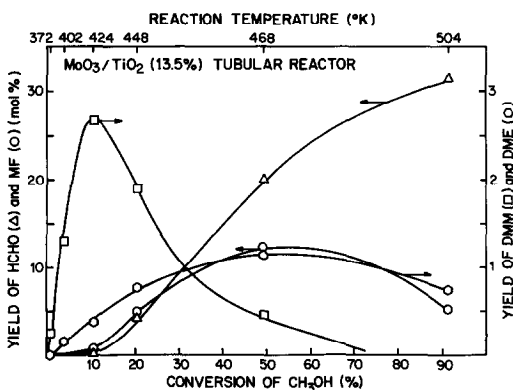
significant amounts of MF are still produced on the 13.5 wt% catalyst, indicating that MF is also produced at molybdenum sites. At present we cannot determine whether this MF production occurs preferentially at the sites on the surface molybdate layer or on the MoO_3 crystallites.

In Fig. 12 we show the yields for the light reaction on the 13.5 wt% MoO_3/TiO_2 catalyst at 403 K. The highest photo-assisted conversion that could be achieved is 16%, compared to the 63% conversion that could be obtained with pure TiO_2. The DMM and MF selectivities are both similar to those seen for the thermal reaction at low conversion, which suggests that the relative rates of the first and second oxidation steps are independent of whether the reaction is thermally or photochemically controlled. The major difference is that CH_2O is not detected in the photo-controlled reaction, indicating again that condensation to produce DMM is strongly favored at the lower temperature. Also, DME is absent as a photoproduct.

The yield vs conversion curves for the photo-controlled reaction on the 4.0 wt% MoO_3/TiO_2 catalyst are nearly identical to those in Fig. 12. This confirms that the MoO_3 crystallites present at the higher loading are photo-inert. It also suggests that
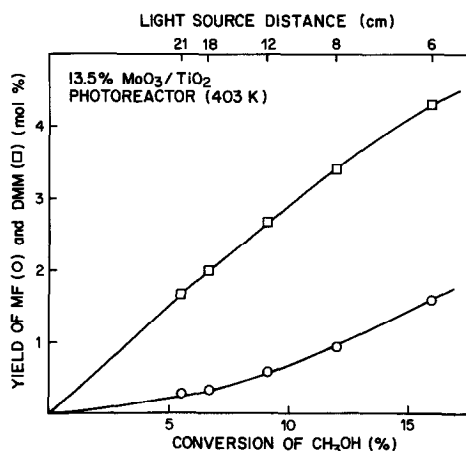

FIG. 11. Intermediate yields for thermally controlled CH_3OH oxidation using 13.5 wt% MoO_3/TiO_2 catalyst.

FIG. 12. Intermediate yields for photo-controlled CH_3OH oxidation using 13.5 wt% MoO_3/TiO_2 catalyst.

the exposed TiO_2 sites in the 4.0 wt% catalyst comprise a small enough fraction of the total surface that their presence does not contribute significantly to the photo-behavior of the catalyst.

DISCUSSION

Catalyst morphology. The spectroscopic and kinetic results for the different Mo loadings (cf. Figs. 2–7) provide convincing evidence that a surface molybdate monolayer is formed in the MoO_3/TiO_2 system. All of the measurements show a transition in behavior at approximately 4.0 wt% MoO_3/TiO_2 loading. As shown in Table 1, this loading corresponds to a surface concentration of 3.6×10^{14} Mo atom/cm^2 of TiO_2. We estimate the relative uncertainty of this number to be ±10%. Thus the saturation coverage of the surface molybdate layer on TiO_2 is comparable to the value for molybdena on Al_2O_3 reported by Weller (4 $\times 10^{14}$ cm^{-2}) (24). This similarity suggests that the packing of the surface molybdate may be insensitive to the structure of the underlying support. We note further that the (001) anatase and (110) rutile crystal planes have surface unit cell densities of 7.0 and 5.4×10^{14} cm^{-2}, respectively (25); these are the principal crystal planes expected in an anatase–rutile mixture (26, 27). Thus we conclude that the surface molybdate layer contains less than one Mo atom per surface unit cell of TiO_2, and may have a stoichiometry as low as one Mo atom per every two surface cells.

The laser Raman spectroscopy results are particularly helpful in demonstrating the molybdena morphology due to the sensitivity of this technique for both small MoO_3 crystallites and noncrystalline molybdena species (21). Thus we can confidently conclude that MoO_3 crystallites are not present in these catalysts until the molybdena loading exceeds approximately 4.0 wt%, and that in catalysts with lower loadings the molybdena is present only as a noncrystalline surface molybdate layer.
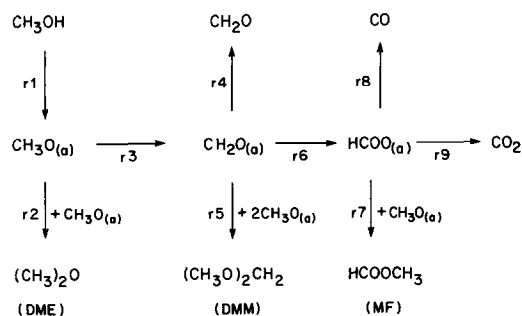
Additional information about the surface

molybdate layer is provided by the coverage dependence of the Raman band 940–970 cm^{-1}. The large width of this band indicates that it is due to transitions within a distribution of vibrational states, rather than a single discrete transition. The coverage dependence of the molybdate Raman band suggests that the local environment of the surface molybdate species is changing with coverage. This suggests that the Mo atoms in the partially completed monolayer are randomly distributed over the TiO_2 surface rather than being present in saturated islands of a surface molybdate phase. Recent *in situ* studies have shown that shifts in Raman bands may be associated with changes in the average number of adsorbed H_2O molecules coordinated to the molybdate species, and that this number is a function of the molybdate coverage (28).

Reaction mechanism. A reaction pathway which can account for our observed kinetic results is given in Scheme 1. For clarity, surface OH species are omitted from this representation.

The first step (r1) is assumed to be the dissociative adsorption of CH_3OH. Spectroscopic evidence for the $CH_3O_{(a)}$ intermediate has been observed on both MoO_3 (29) and TiO_2 (30), and the analogous $C_2H_5O_{(a)}$ intermediate has been reported on MoO_3 supported on SiO_2 (31).

The $CH_3O_{(a)}$ intermediate can then react via either an oxidative or nonoxidative channel. In the nonoxidative channel, it reacts with a neighboring $CH_3O_{(a)}$ group or

CH$_3$OH   CH$_2$O   CO

r1   r4   r8

$CH_3O_{(a)}$ —r3→ $CH_2O_{(a)}$ —r6→ $HCOO_{(a)}$ —r9→ CO_2

r2 +CH$_3$O$_{(a)}$ r5 +2CH$_3$O$_{(a)}$ r7 +CH$_3$O$_{(a)}$

$(CH_3)_2O$ $(CH_3O)_2CH_2$ HCOOCH$_3$
(DME)   (DMM)   (MF)

SCHEME 1

physically adsorbed CH_3OH molecule to produce the condensation product DME (r2). The reaction occurs thermally on both TiO_2 and the surface molybdate catalysts, but it cannot be photo-excited on either catalyst.

The oxidative channel involves H-atom abstraction from $CH_3O_{(a)}$ to produce a transient adsorbed $CH_2O_{(a)}$ intermediate (r3). This has been shown to be the rate-limiting step on MoO_3 and Fe_2O_3–MoO_3 methanol oxidation catalysts (8). Our results show that this step can be photo-excited on both TiO_2 and the surface molybdate catalyst. The mechanism of the photo-excited reaction probably involves hole capture at a surface O^{2-} anion to produce a surface $O^{·-}$ species, which then abstracts an H atom from a neighboring $CH_3O_{(a)}$ group (32).

The $CH_2O_{(a)}$ intermediate can then react via one of three channels: desorption, condensation, or further oxidation. Desorption (r4) is the major thermal reaction on the 13.5 wt% catalyst above 450 K (cf. Fig. 11). Desorption also occurs with about 33% selectivity on TiO_2 under photo-controlled conditions (cf. Fig. 9).

The condensation reaction results in the formation of DMM (r5). This is the major reaction on the molybdate catalysts at low conversion (cf. Figs. 10–12), and occurs with about 10% selectivity on TiO_2 under photo-controlled conditions (cf. Fig. 9). The reaction is favored by low temperatures, as indicated by the simultaneous decrease in DMM yield and increase in CH_2O yield as temperature is increased for the thermally controlled reaction (cf. Figs. 10, 11). We note that the sum of the DMM and CH_2O yields is nearly linear with respect to conversion through the low-temperature region, which indicates that both products originate from the same $CH_2O_{(a)}$ intermediate. The condensation mechanism is probably analogous to that for acetal formation (33), with nucleophilic attack by the O atoms of two neighboring $CH_3O_{(a)}$ or CH_3OH species onto the C atom of the $CH_2O_{(a)}$ intermediate.

The oxidation channel involves the immediate conversion of the $CH_2O_{(a)}$ intermediate into an adsorbed formate species (r6). This reaction has already been shown to occur on ZnO surfaces (34). Evidence that it occurs on TiO_2 under photo-controlled conditions is seen in the yield plot for MF (cf. Fig. 9), which is linear with respect to conversion of CH_3OH. The absence of positive curvature indicates that MF is a primary oxidation product under these conditions. This in turn indicates that the rate of the oxidation step (r6) is first order in $CH_2O_{(a)}$ concentration, and that the subsequent reaction to produce MF (r7) is fast. The mechanism for the oxidative channel probably involves nucleophilic attack at the C atom in the $CH_2O_{(a)}$ intermediate by a neighboring O^{2-} surface anion.

We note that these results do not eliminate the possibility that MF is also produced via CH_2O disproportionation at higher conversions.

The final steps in Scheme 1 involve the decomposition of the formate intermediate. Again, three channels are available: condensation to produce MF (r7), direct decomposition to produce CO (r8), and oxidative decomposition to yield CO_2 (r9). We cannot comment on the selectivity ratio r8/r9, since the product concentrations of CO and CO_2 were not measured in this work. However, a carbon balance on the products indicates that hydrogen-containing species make up all of the product spectrum below 450 K. Thus, the ratio (r7)/(r8 + r9) is large at low temperature. This confirms one of the initial goals of this study, namely the use of photoexcitation to activate the primary oxidation step at low enough temperature to suppress the formation of higher oxidation products. Additional work is planned to determine conditions for optimizing this effect.

SUMMARY

(1) Molybdena supported on TiO_2 is present as a surface molybdate monolayer

at loadings less than 4×10^{14} cations/cm^2. At higher loadings the additional molybdena is present as MoO_3 crystallites.

(2) In the oxidation of CH_3OH on both TiO_2 and the surface molybdate catalysts, the primary oxidation step is H-atom abstraction from an adsorbed $CH_3O_{(a)}$ species.

(3) On TiO_2, the resulting $CH_2O_{(a)}$ intermediate is primarily converted to $HCOO_{(a)}$, leading to the desorption of MF as the major photo-oxidation product.

(4) On molybdena/TiO_2 at 403 K, the $CH_2O_{(a)}$ intermediate condenses with neighboring $CH_3O_{(a)}$ groups to produce DMM as the major photo-oxidation product.

(5) Desorption of CH_2O *does* occur as the primary product at higher temperatures on the molybdena/TiO_2 catalysts, and under photo-controlled conditions from a minority fraction of the TiO_2 surface sites.

(6) The formation of CO and CO_2 on TiO_2 catalysts is significantly reduced by operating under photo-controlled reaction conditions.

(7) For CH_3OH oxidation, the selectivity of the primary oxidation step is insensitive to excitation mechanism. However, overall selectivity is strongly influenced by the reaction temperature and its effect on surface coverages during reaction following the primary oxidation step.

ACKNOWLEDGMENT

REFERENCES

1. Bickley, R. I., "Chemical Physics of Solids and Their Surfaces" Vol. 7 (Specialist Periodic Reports, the Chemical Society, London, 1978), p. 118.

2. Cunningham, J., and Hodnett, B. K., *J. Chem. Soc. Faraday Trans. 1* **77,** 2777 (1981).

3. Djeghri, N., and Teichner, S. J., *J. Catal.* **62,** 99 (1980).

4. Pichat, P., Herrmann, J. M., Disdier, J., and Mozzanega, M. N., *J. Phys. Chem.* **83,** 3122 (1979).

5. Cundall, R. B., Rudham, R., and Salim, M., *J. Chem. Soc. Faraday Trans. 1* **72,** 1642 (1976).

6. Ai, M., *J. Catal.* **54,** 426 (1978).

7. Ai, M., *J. Catal.* **83,** 141 (1983).

8. Machiels, C. J., and Sleight, A. W., *J. Catal.* **76,** 238 (1982).

9. Grasselli, R. K., and Burrington, J. D., "Advances in Catalysis," Vol. 30, p. 133. Academic Press, New York, 1981.

10. Keulks, G. W., Krenzke, L. D., and Notermann, T. M., "Advances in Catalysis," Vol. 27, p. 183. Academic Press, New York, 1978.

11. Fransen, T., VanBerge, P. C., and Mars, P., *in* "Preparation of Catalysts" (B. A. Delmon, P. A. Jacobs, and G. Poncelet, Eds.), Vol. 1, p. 405. Elsevier, Amsterdam, 1976.

12. Nag, N. K., Fransen, T., and Mars, P., *J. Catal.* **68,** 77 (1981).

13. Ono, T., Nakagawa, Y., Miyata, H., and Kubokawa, Y., *Bull. Chem. Soc. Jpn.* **57,** 1205 (1984).

14. Massoth, F. E., "Advances in Catalysis," Vol. 27, p. 265. Academic Press, New York, 1978.

15. Akimoto, M., and Echigoya, E., *J. Catal.* **29,** 191 (1973).

16. Vanhove, D., Op, S. R., Fernandes, A., and Blanchard, M., *J. Catal.* **57,** 253 (1979).

17. Okazaki, S., Kunasaka, M., Yoshida, J., Kosaka, K., and Tanabe, K., *I&EC Prod. Res. Dev.* **20,** 301 (1981).

18. Matsuda, S., and Kato, A., *Appl. Catal.* **8,** 149 (1983).

19. Chan, S. S., Wachs, I. E., Murrell, L. L., and Dispenziere, N. C., *J. Catal.* **92,** 1 (1985).

20. Chan, S. S., and Bell, A. T., *J. Catal.* **89,** 433 (1984).

21. Jeziorowski, H., and Knozinger, H., *J. Phys. Chem.* **83,** 1166 (1979).

22. Beattie, I. R., and Gilson, T. R., *J. Chem. Soc.* (a) 2322 (1969); *Proc. R. Soc. London Ser. A* **307,** 407 (1968).

23. Krylov, O. V., "Catalysis by Nonmetals." Academic Press, New York, 1970.

24. Weller, S. A., *Acc. Chem. Res.* **16,** 101 (1983).

25. Wyckoff, R. G., *in* "Crystal Structures," Vols. I, II. Interscience, New York, 1964.

26. Boehm, H. P., "Advances in Catalysis," Vol. 16, p. 179. Academic Press, New York, 1966.

27. Jones and Hackey, *Trans. Faraday Soc.* **67,** 2679 (1971).

28. Chan, S. S., Wachs, I. E., Murrell, L. L., Wang, L., and Hall, W. K., *J. Phys. Chem.* **88,** 5831 (1984).

29. Ohuchi, F., and Chowdhry, A., Proceedings of 12th North American Thermal Analysis Society Conference (Williamsburg, VA, 1983) paper 103.

30. Carrizosa, I., Munuera, G., and Castanar, S., *J. Catal.* **49,** 265 (1977).

31. Ueno, A., Onishi, T., and Tamaru, K., *Trans. Faraday Soc.* **67,** 3585 (1971).

32. Che, M., and Tench, A. J., "Advances in Catalysis," Vol. 31, p. 77. Academic Press, New York, 1982.

33. Allinger, N. L., Cava, M. P., deJongh, D. C., Johnson, C. R., Lebel, N. A., and Stevens, C. L., "Organic Chemistry" (Worth Publishers, New York, 1971) p. 476.

34. Chan, L., and Griffin, G. L., submitted for publication.